IEEE Open Journal of
Antennas and Propagation

Received 23 August 2021; accepted 20 September 2021. Date of publication 24 September 2021; date of current version 1 October 2021.

Digital Object Identifier 10.1109/OJAP.2021.3115342

Fixed-Frequency Beam-Steering Using Slotted Waveguide With Tunable Impedance Walls

AMIRMASOUD OHADI (Student Member, IEEE), AND GEORGE V. ELEFTHERIADES (Fellow, IEEE)

Edward S. Rogers Sr. Department of Electrical and Computer Engineering, University of Toronto, Toronto, ON M5S 3G4, Canada

CORRESPONDING AUTHOR: A. OHADI (e-mail: s.ohadi@mail.utoronto.ca)

ABSTRACT In this paper, we describe the development of a new beam-steerable antenna array using a reconfigurable waveguide with tunable impedance side walls. The array has 36 radiating elements placed on the top wall of the waveguide and a common biasing voltage for tuning the impedance walls. The antenna operates at 9.3 GHz and its beam can be steered from 22° to 65° by changing the bias voltage from 16 to 7 volts. The gain of the antenna remains within the 3 dB limit of the maximum gain of 11.8 dB throughout the steering range. The effective radiating length of the antenna is 13λ and its half-power beamwidth is 5°. For this frequency range and electrical length, this antenna has a high radiation efficiency. This is due to the phase-shifting mechanism used which results in the varactor loss being less than all other sources of loss throughout most of the steering range. This makes the antenna suitable for applications where the varactors should operate at high frequencies with relatively low quality factors.

INDEX TERMS Antennas, beam steering, impedance wall, leaky-wave, metasurface, phase shifting, slot arrays, varactors.

I. INTRODUCTION

THE NEED for fixed-frequency beam-steerable antennas has been increasing due to their growing applications in high-speed communications, imaging systems, radars, and remote sensing [1]–[3]. In particular, many recent research works have focused on designing low-cost, easily extendable, beam-steerable antennas with large steering ranges. In order to introduce tunability to an antenna at a fixed-frequency, tunable electronic components such as varactors or MEMS capacitors are employed [4]–[8]. These tunable electronic elements often have two major limitations, their tunability range and their quality factor, both of which become worse at higher frequencies. These limitations impose constraints on the range and the efficiency of the phase-shifting mechanism in the antenna.

One versatile approach to reconfigurability is by using phased arrays where one can control both the amplitude and the phase of each radiating element [9]–[10]. Therefore, one can change the angle of radiation and the shape of the beam simultaneously. However, the versatility of phased arrays comes at the cost of a complex feed network, the cost associated with the transceiver behind each antenna element, and the associated DC power consumption. These hurdles make the extension of phased arrays complicated when a larger array is needed for a higher gain and a smaller beamwidth.

Alternative approaches include manipulating electromagnetic waves using reconfigurable metasurfaces. Metasurfaces are composed of sub-wavelength unit cells (meta-atoms) and can be used to transform arbitrary incident electromagnetic waves to a desired transmitted wave [11]. This can be done by designing the unit cells to satisfy the boundary conditions at the interface between the two sides of the metasurface. One important challenge in the design of metasurfaces for beam-steering applications is to minimize the reflection loss. This can be done by using Huygens' metasurfaces. In Huygens' metasurfaces, the direction and the amplitude of the electric and magnetic dipoles are perpendicular and weighted such that the reflected radiation can be minimized [12]. In order to introduce tunability to a metasurface, one needs to load the meta-atoms with tunable electronic elements such that the designed reconfigurable unit cells can provide the desired impedance range with a high transmission efficiency [13].

On the other hand, transmitarrays and reflectarrays can also be used for 2D fixed-frequency beam steering [14]–[16]. The phase-shifting mechanism is through individual tuning

of the reconfigurable transmitarray or reflectarray elements that are larger than metasurface unit cells (in the order of the operating frequency wavelength). However, the drawback of this method is that one needs to excite the transmitarray with an external antenna which makes the system bulky and introduces considerable spillover loss. In addition, each radiating element needs an individual bias voltage. This makes extending the antenna size complicated as the number of voltage bias lines grows as N^2, where N is the number of radiating elements in one dimension.

In order to have the benefit of a simple feed network and a simple bias voltage circuitry simultaneously, one can use tunable leaky-wave antennas. Leaky-wave antennas have been conventionally used for frequency scanning due to their simple feed network and phase-shifting mechanism [17]–[18]. By periodically loading a conventional leaky-wave antenna with a tunable electronic element, one can utilize the leaky-wave antenna for fixed-frequency beam steering [19]–[20]. Due to the series feeding scheme in leaky-wave antennas, the loss is accumulated as the wave propagates in the waveguide. Therefore, one important challenge in the design of beam-steerable leaky-wave antennas is to improve their radiation efficiency. This becomes even more important at higher frequencies where the quality factor of the tunable electronic elements drops substantially. Moreover, increasing the radiation efficiency of fixed-frequency beam-steerable leaky-wave antennas proves crucial when a narrow beamwidth and a large electrical length is needed.

In this paper, we introduce a new beam-steerable leaky-wave antenna based on tunable Huygens' metasurfaces. The proposed leaky-wave antenna has a simple feed network and bias circuitry with only one common bias voltage. The presented antenna combines standard waveguide slot arrays (in leaky-wave operation mode [21]) with metasurface (impedance wall) waveguides. Specifically, the proposed phase-shifting mechanism is based on two tunable phase-shifting walls placed on the two sides of a rectangular waveguide. To the best of our knowledge, the antenna has one of the highest reported efficiencies for a radiating length of 13λ among other tunable leaky-wave antennas operating at 6 GHz or above with similar antenna electrical length. This is due to the designed phase-shifting mechanism which makes the varactor loss less than all other losses and makes it possible to manage them at a relatively high frequency with a lower quality factor compared to lower frequencies. Preliminary simulation results for the proposed antenna were published in [22]. In this paper, we investigate the theory of the proposed antenna as well as the measurement results of a prototype which was fabricated using CNC machining.

II. TUNBLE IMPEDANCE WALL

An ideal phase-shifting impenetrable wall introduces a desired phase-shift of ζ to an incident plane wave with an incident angle of θ_i, and reflects it with the same angle of reflection θ_r as the incident angle (see Fig. 1 for the case of a TE incident plane wave). Assuming an impenetrable

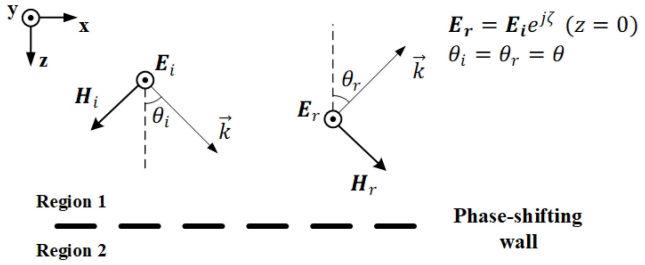

FIGURE 1. TE plane wave incident on a phase-shifting wall. E_i and H_i are the incident electric and magnetic field vectors respectively. E_r and H_r are the reflected electric and magnetic field vectors respectively.

surface (zero 2), the electric impedance of a phase-shifting wall can be found using (1), where $\mathbf{E}_1$ is the electric field vector and $\mathbf{H}_1$ is the magnetic field vector in region 1 on the phase-shifting wall as shown in Fig. 1 ($\mathbf{t}$ denotes tangential component) [23]. $\mathbf{Z}_s$ is the electric impedance tensor. Whereas $\hat{\mathbf{n}}$ is the vector normal to the surface pointing from region 2 towards region 1.

$$\hat{\mathbf{n}} \times \mathbf{H}_1 = \mathbf{Z_s}^{-1} \times \mathbf{E^t}_1 \tag{1}$$

Assuming a TE incident plane wave as illustrated in Fig. 1, the electric and magnetic fields in region 1 can be found from (2)-(3).

$$\mathbf{E}_1 = \mathbf{E}_i + \mathbf{E}_r \tag{2}$$

$$\mathbf{H}_1 = \mathbf{H}_i + \mathbf{H}_r \tag{3}$$

The relations for the incident fields, $\mathbf{E}_i$ and $\mathbf{H}_i$, and the reflected fields, $\mathbf{E}_r$ and $\mathbf{H}_r$, can be found from (4)-(7).

$$\begin{cases} \mathbf{E}_i = E_0 e^{-jkcos\theta z} e^{-jksin\theta x} \hat{y} & (4) \\ \mathbf{E}_r = E_0 e^{j\zeta} e^{+jkcos\theta z} e^{-jksin\theta x} \hat{y} & (5) \\ \mathbf{H}_i = \frac{E_0}{\eta} e^{-jkcos\theta z} e^{-jksin\theta x} (sin\theta \hat{z} - cos\theta \hat{x}) & (6) \\ \mathbf{H}_r = \frac{E_0}{\eta} e^{j\zeta} e^{+jkcos\theta z} e^{-jksin\theta x} (sin\theta \hat{z} + cos\theta \hat{x}) & (7) \end{cases}$$

Evaluating the incident and reflected fields at the surface ($z = 0$) and using them in equation (1) results in the relation for the electric impedance of the ideal phase-shifting wall given by (8). As the equation is purely imaginary, ideal phase-shifting walls can be implemented as a passive and lossless metasurface to introduce a desired phase-shift to a TE plane wave with an arbitrary angle of incidence.

$$Z_s = j \frac{\eta}{cos\theta} cot\frac{\zeta}{2} \tag{8}$$

Ideally, the electric impedance of a metasurface does not change by varying the incident angle [23]. Therefore, given an impenetrable phase-shifting wall designed to introduce a phase-shift of ζ_0 to a TE plane wave with an incident angle of θ_0, one can derive the phase-shift ζ_1 introduced by the designed phase-shifting wall to a TE plane wave with a different incident angle θ_1. This can be done by equating the right hand side of equation (8) for the two cases which results in equation (9).

$$cos\theta_1 \, tan\frac{\zeta_1}{2} = cos\theta_0 \, tan\frac{\zeta_0}{2} \tag{9}$$

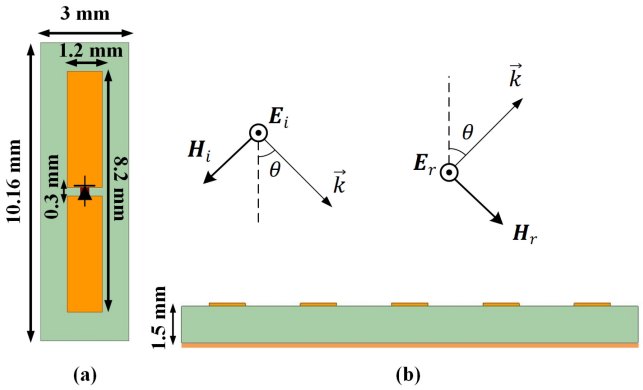

FIGURE 2. Structure of the designed phase-shifting wall (a) Top view. (b) Side view with the relative directions of the incident fields.

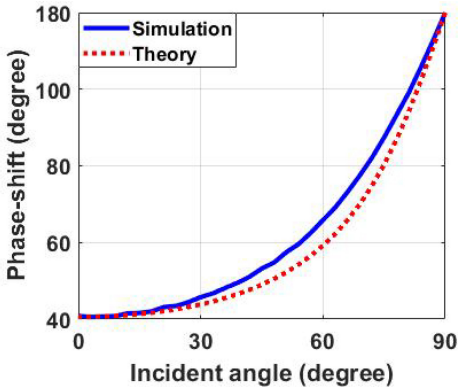

FIGURE 3. Calculated and simulated results for the phase-shift introduced to oblique TE plane waves with different incident angles on the designed phase-shifting wall.

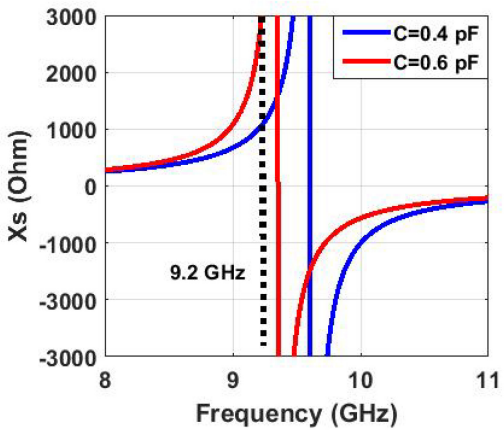

FIGURE 4. The impedance of the designed phased-shifting wall vs. frequency.

In order to verify that equations (8)-(9) are valid for practical non-ideal impedance surfaces, we designed a phase-shifting wall that introduces 40° phase-shift to a normal TE incident plane wave at 9.2 GHz by arranging dipoles on a grounded substrate. Using the design values in (8) yields $X_s = 1036$ Ohm, where X_s is the imaginary part of Z_s. As shown in Fig. 2, the unit cell of the wall consists of a dipole on a substrate with a varactor located in the gap in the middle of it. The dimensions of the unit cell are shown in Fig. 2. Choosing dipoles as the unit cell components allows minimizing the number of varactors while providing sufficient impedance range. This is achieved by having only one unit cell along the y axis where there is no change in the electric and magnetic fields. However, the width of the unit cell is chosen to be less than $\lambda/10$ along the propagating direction (x axis) to make the assumption of a homogeneous impedance surface a good approximation. The substrate is Rogers 3003 with relative permittivity of 3 and a thickness of 1.5mm with a PEC on the bottom surface. The capacitance of the varactor is 0.4 pF. For simplicity, we have only used a capacitor instead of the varactor. A complete varactor model will be used later for a detailed characterization in Section IV.

Using 0° and 40° for θ_0 and ζ_0 in (9) respectively, results in (10) which is the relation for the phase-shift ζ introduced to an oblique TE plane wave incident at an arbitrary angle of θ on the designed phase-shifting wall. Fig. 3 compares the calculated phase-shifts for different incident angles using equation (10) with those derived from the full-wave High-Frequency Structure Simulator (HFSS). We can see a very good agreement between the two.

$$\zeta = 2\, tan^{-1}(tan(20°)\, sec\theta) \tag{10}$$

Contrary to an ideal impedance wall, the impedance of the designed phase-shifting wall changes with frequency due to the changing impedance of the varactors and the changing electrical length of the dipoles with frequency. Fig. 4 shows the impedance of the wall from 8 GHz to 11 GHz for two different varactor capacitance values. As shown, at lower frequencies, the surface impedance increases as we increase the frequency until we reach the resonance frequency where the wall has a very large impedance. This large impedance corresponds to a 0° phase-shift to all incoming TE plane waves according to (8). In practice, we need to avoid operating very close to the resonance frequency as the loss is increased and the efficiency is degraded dramatically in this frequency range.

As shown in Fig. 4, increasing the capacitance of the varactor decreases the resonance frequency, which in return, increases the surface impedance throughout the frequency range. It is shown that at the designed frequency of 9.2 GHz, by changing the capacitance from 0.4 pF to 0.6 pF, Xs changes from 1036 Ohm to 2474 Ohm. This in return, changes the phase-shift introduced to a normal TE incident plane wave from 40° to 17° as implied by (8). In this way, by using a varactor in the middle of a dipole, one can make a tunable phase-shifting wall and characterize it for all incident angles and frequencies using equation (8).

III. RECONFIGURABLE WAVEGUIDE WITH TUNABLE IMPEDANCE WALLS

An electromagnetic wave is guided in a rectangular waveguide by bouncing back and forth with a certain angle between the two side walls through successive reflections (see Fig. 5). The modal configuration and the dispersion relation in a

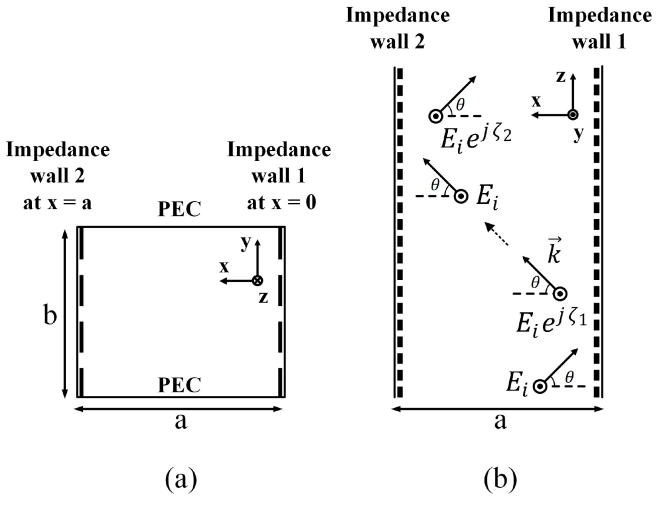

FIGURE 5. TE wave propagation inside a rectangular waveguide with phase-shifting walls. a. Transverse cross-section b. View from the top.

rectangular waveguide depend on the distance between the walls and the phase-shift introduced to the reflected wave by them. In [24] and [25], the propagation of electromagnetic waves in a rectangular waveguide with impedance walls is comprehensively studied. However, the purpose of this manuscript is to study a reconfigurable impedance-wall waveguide and to use it as a beam-steerable leaky-wave antenna. Therefore, we provide a concise analysis which suites the proposed design and enables us to easily study the effect of different parameters on the performance of the beam-steerable antenna.

Equation (11) is the general transverse resonance condition for an arbitrary rectangular waveguide with a propagating TE mode. ζ_1 and ζ_2 are the phase-shifts from the two side-walls, n is the mode number which is 0 for the first propagating mode, k_x is the transverse wave number in the waveguide, and a is the distance between the two phase-shifting walls.

$$\zeta_1 + \zeta_2 - 2k_x a = 2n\pi \tag{11}$$

Assuming identical phase-shifting walls on both sides and given the fact that we are interested in the first propagating mode, (11) can be written in a simpler form as (12).

$$\zeta = k_x\, a \tag{12}$$

Using (12) in (8), to substitute for ζ, results in equation (13) that is a transcendental equation from which we can find the transverse wave number k_x for any possible eigenmode solution (ω), and hence the dispersion relation of the waveguide. X_s is the imaginary part of the surface impedance Z_s and μ is the permeability of vacuum. It should be noted that X_s is generally a function of frequency.

$$cot(\frac{k_x a}{2}) = \frac{X_s}{\omega\mu}\, k_x \tag{13}$$

Knowing k_x, the corresponding longitudinal wave number β can be found from (14) where k_0 is the wave number in vacuum.

$$\beta = \sqrt{k_0^2 - k_x^2} \tag{14}$$

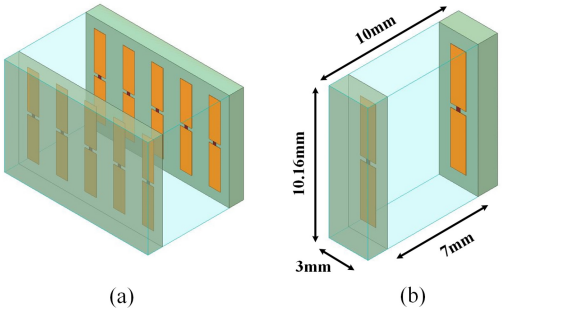

FIGURE 6. a. Reconfigurable waveguide structure. b. One unit cell of the waveguide.

In addition to the dispersion relation, it is also beneficial to find the electric and magnetic field modal configurations in the waveguide. For this purpose, one needs to solve Maxwell's equations in the waveguide with the following boundary conditions as depicted in Fig. 5.a.

$$\frac{E_y}{-H_z}\Big|_{x=0} = Z_s,\ \frac{E_y}{H_z}\Big|_{x=a} = Z_s \tag{15}$$

$$E_{x,z}\Big|_{y=0,b} = 0 \tag{16}$$

In order to find the fields for the first propagating mode, TE_{10}, we assume no change along the y-axis. This results in (17) as the relation for the transverse electric field in the waveguide. The transverse and longitudinal components of the magnetic field can be found from (18)-(19). Transverse and longitudinal wave numbers can also be found from (13) and (14) respectively. Equations (17)-(19) show that the electric and magnetic fields are symmetric truncated forms of the TE_{10} mode in a simple rectangular waveguide with four PEC walls. This makes sense since essentially one can view the walls as shorted stubs and replace them with an equivalent inductance.

$$\begin{cases} E_y = E_0\, cos(k_x(x - \frac{a}{2}))e^{-j\beta z} \\ H_x = -\frac{\beta}{\omega\mu}E_0\, cos(k_x(x - \frac{a}{2}))e^{-j\beta z} \\ H_z = \frac{jk_x}{\omega\mu}E_0\, sin(k_x(x - \frac{a}{2}))e^{-j\beta z} \end{cases}$$

In order to implement the reconfigurable waveguide, we placed the designed phase-shifting walls (see Fig. 2) on the two sides of a waveguide (see Fig. 6). We used the impedance of the designed phase-shifting wall as a function of frequency (see Fig. 4) in (13) to find the dispersion relation in the waveguide. Although the width of the waveguide is 10mm, the thickness of each impedance sheet is 1.5mm which should be excluded resulting in a = 7mm in (13). Fig. 7 compares the dispersion relation found using (13) with that derived from an HFSS eigenmode simulation for one unit cell with 0.4 pF as the varactor capacitance. As shown, equation (13) provides a very good approximation for the dispersion in the waveguide with non-ideal impedance walls which matches very well with the simulation result.

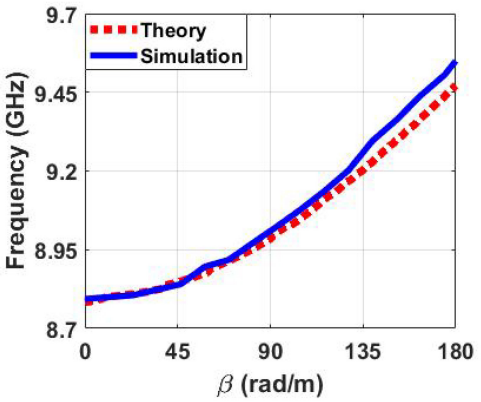

FIGURE 7. Dispersion diagram for the waveguide with non-ideal impedance walls.

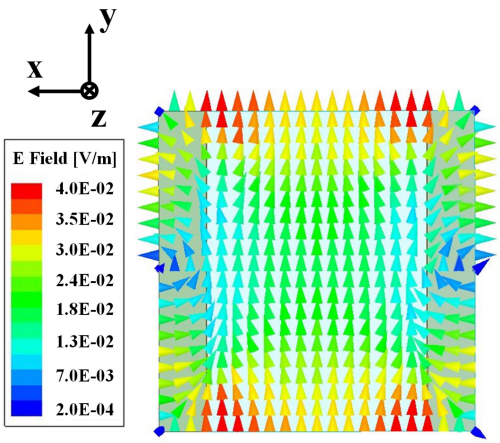

FIGURE 8. Electric field in the waveguide with non-ideal impedance walls.

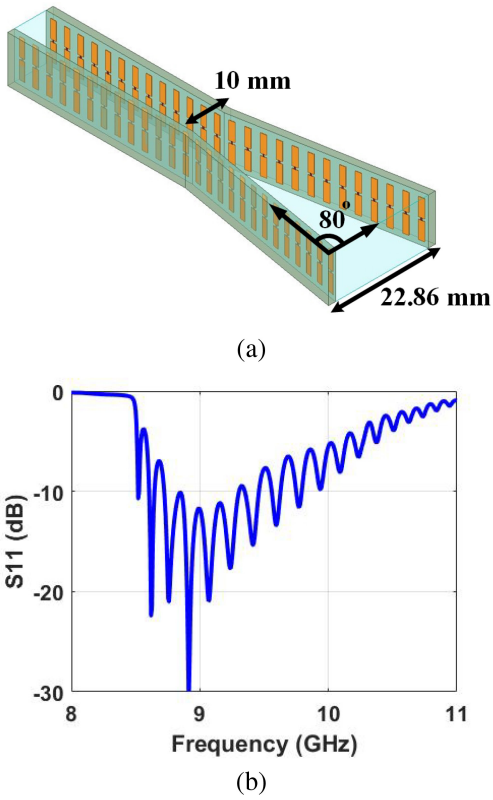

FIGURE 9. a. The tapered section which connects the regular WR90 (front face) to the designed waveguide with impedance walls (back face). b. The return loss when excited by a regular WR90 waveguide.

Fig. 8 shows the electric field of the first propagating mode at 9.2 GHz in the designed waveguide with non-ideal impedance walls when the capacitance is 0.4 pF. The phase reference for the impedance walls is the outer face of the substrate where the dipoles are located. Therefore, we expect a truncated TE_{10} modal configuration ($E_x = 0$) between the outer surfaces of the impedance walls as can be seen in Fig. 9. Interestingly, field inside the substrate is E_x which is curling around the center of the side walls. This time-variable curling electric field is the cause of the magnetic response of the impedance wall while the electric response is attributed to the induced current on the dipoles. As shown in Fig. 8, the electric field configuration between the two impedance walls is not as simple as the case with ideal impedance walls. This is due to the fact that the assumption of $\frac{\partial}{\partial y} = 0$ is not valid with the non-ideal phase-shifting walls and the electric field changes in magnitude along the y axis. But the modal configuration becomes more similar to that of the ideal case as we move away from the top and bottom walls towards the middle of the waveguide where the edge effect is weakened. In this region, the electric field is maximum in the middle and decreases along the x axis in the form of a truncated sinusoid as expected from (17).

The last step is to design the excitation and termination of the waveguide with impedance walls. One can use a standard rectangular waveguide that supports the desired frequency for this purpose. As the standard waveguide has PEC side walls with 180° phase-shift, it needs to have a larger width compared to the waveguide with phase-shifting walls to support the desired frequency. On the other hand, the transverse electric and magnetic fields are zero on the two side walls of the standard waveguide. Therefore, placing the designed impedance walls on the two sides of it does not change the modal configuration as long as the thickness of the substrate is small. This suggests that we can match the waveguide with impedance walls to the standard waveguide by tapering the width of the former and increase it to reach the width of the latter while keeping the impedance walls on the two sides. Fig. 9.a shows the tapered section connecting the designed waveguide with phase-shifting walls to a standard WR90 waveguide which can be used for excitation and termination. Fig. 9.b shows the simulation result for the return loss of the designed waveguide versus frequency when it is excited by a standard WR90 waveguide through the designed tapered section and the varactor capacitance is 0.6 pF.

By varying the capacitance of the varactors, one can change the impedance of the phase-shifting walls as discussed in Section II and in return, change the electric field modal configuration and its corresponding longitudinal wave number in the waveguide. In this way, the designed reconfigurable waveguide can be used as a tunable distributed phase-shifter. Moreover, by placing slots on the top wall,

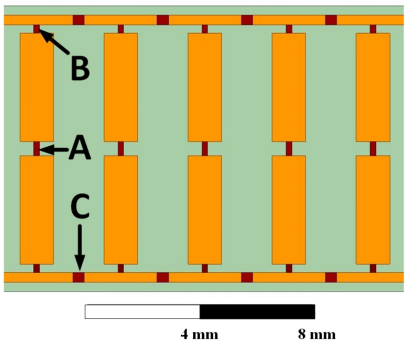

FIGURE 10. The complete structure of the impedance wall. A is the location of the varactor, B is the location of the decoupling 887 kOhm resistor, and C is the location of the 1 kOhm resistor.

we can use it for beam-steering. In this paper we will focus on the beam-steering application.

In the following sections we will investigate the practical implementation of the designed reconfigurable waveguide as a fixed-frequency beam-steerable slotted antenna. For this purpose, we have to design the bias circuitry and characterize the varactors.

IV. BIAS CIRCUITRY AND VARACTOR CHARACTERIZATION

The DC bias voltages of all the varactors are the same and is provided by two lines with a width of 0.3 mm placed above and below the dipoles carrying VDD and GND respectively. These two DC bias lines are extended along the waveguide on each of the phase-shifting walls. As the diodes are reverse-biased, their DC current is negligible and very large resistors can be used to connect each side of a dipole to the corresponding DC bias line without disturbing the DC voltages. We used 887 kOhm resistors to resemble an open circuit and to maximize the decoupling between the dipoles and the DC bias lines for the AC signal. The DC bias lines can act as a transmission line and introduce their own propagating mode inside the waveguide. In order to keep the waveguide single-moded at the operating frequency, we need to suppress this propagating mode on the DC bias lines. For this purpose, we periodically loaded the bias lines with 1 kOhm resistors. This eliminates the undesired mode while it does not change the DC bias voltages as only a very small current is passing through the added resistors. Furthermore, the bias lines do not change the desired mode in the waveguide as they are oriented perpendicularly to the electric field direction. The final topology of the phase-shifting walls including the bias circuitry is shown in Fig. 10.

In order to characterize the MAVR-120 varactor used for fabrication, we used its SPICE model provided by the manufacturing company in the circuit schematic shown in Fig. 11. The SPICE model does not mention the value of the parasitic inductance which proves very important at our operating frequency. In order to find its value, we fabricated and placed a piece of the designed phase-shifting wall at the end of a WR90 waveguide and measured the introduced phase-shift to the incident waves at different frequencies. We also used the

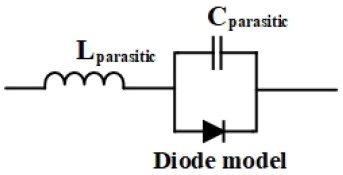

FIGURE 11. The varactor model used for the simulations. The diode model as well as the parasitic capacitance are given in the manufacturer's data sheet.

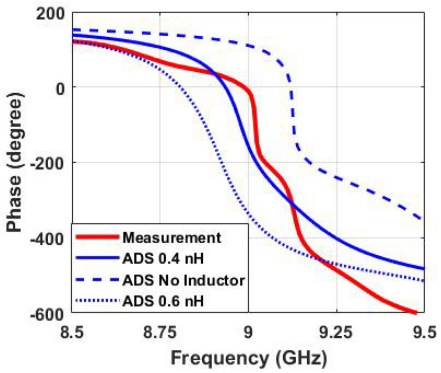

FIGURE 12. Measurement and simulation results for the phase-shift from a piece of the designed impedance wall placed at the end of a WR90 waveguide.

TABLE 1. Values for the MAVR120 varactor model used in HFSS.

Voltage [V]	Capacitance [pF]	Resistance [Ω]	Quality factor
4	0.80	1151	56
6	0.49	5117	144
8	0.36	14340	300
10	0.3	29560	518
12	0.27	58340	894
14	0.24	104400	1457

SPICE model with different values of the parasitic inductance and compared the Advanced Design System (ADS) simulation results with the measurement results. Fig. 12 shows that a series inductance of 0.4 nH provides a good model and matches very well with the measurement result.

Adding a 0.4 nH parasitic inductor to the SPICE model of the varactor, we modeled the whole device as a parallel combination of a capacitor and a resistor to use it in HFSS simulations. The corresponding circuit element values for different DC bias voltages and their associated quality factors at 9.2 GHz are tabulated in Table 1.

As shown in Table 1, decreasing the voltage decreases the quality factor dramatically. This is due to the fact that by decreasing the voltage, the capacitance increases which in return deceases the self-resonance frequency of the varactor and makes it closer to our operating frequency at 9.2 GHz. Therefore, we need to avoid using the varactor for voltages lower than 7V as it decreases the efficiency substantially.

It is also useful to investigate the effect of the operating frequency on the quality factor of the varactors. Fig. 13 shows the quality factor of MAVR120 varactors as we change the frequency from 5GHz to 10GHz for two different DC bias voltages. As shown, the quality factor decreases substantially as we increase the frequency and operate closer to the self-resonance frequency of the varactors for both bias voltages.

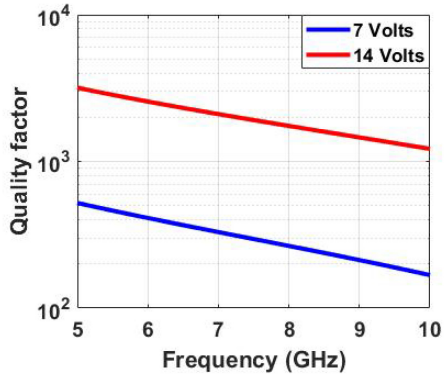

FIGURE 13. The quality factor of the MAVR120 varactor versus frequency for different bias voltages.

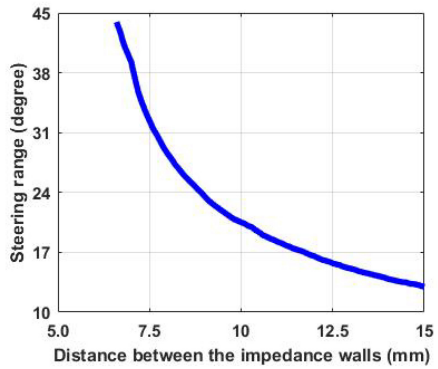

FIGURE 14. The steering range versus the distance between the two phase-shifting walls 'a'.

This effect is so significant such that depending on the bias voltage, the quality factor of the varactor at 10 GHz is smaller by a factor of 3 to 5 times compared to that at 5 GHz.

V. SCANNING RANGE AND ARRAY DESIGN

The steering range of an array can be found from (20) [26]. In the designed reconfigurable waveguide, the longitudinal wave number β can be changed by tuning the bias voltage of the varactors. The capacitance range of the varactors is limited from above to 0.45 pF by their quality factor, and from below to 0.22 pF by the reverse breakdown voltage. This limits the available surface impedance range between 2500 and 982 Ohm at 9.2 GHz.

$$\theta = sin^{-1}\left(\frac{\beta}{k_0}\right) \tag{20}$$

Given the minimum and maximum values of the surface impedance at our desired operating frequency and using equations (13) and (20), one can find the steering range as a function of the distance between the two phase-shifting walls. As shown in Fig. 14, the steering range is increased as the distance between the two phase-shifting walls is decreased. For distances less than 6.8mm, β becomes purely imaginary and hence the eigenmode is evanescent. Therefore, we chose the separation of the two impedance walls to be 7mm in order to maximize the steering range. As a result, for the designed waveguide, the beam is steered from 60° to 20° by changing the bias voltage from 7 to 16 Volts.

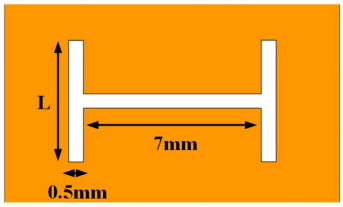

FIGURE 15. The H-shaped loaded slot structure.

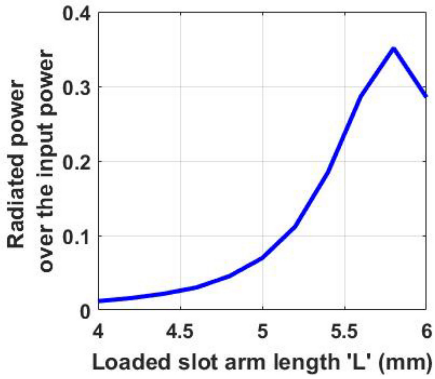

FIGURE 16. Radiated power over the incident power for different arm lengths L.

As 7mm is less than half-wavelength at our operating frequency, we use H-shaped loaded slots on the top wall as radiating elements to achieve sufficient radiated power with smaller slot length. We do not use longitudinal slots for two reasons. Firstly, their gain drops rapidly in the scanning plane near the grazing angle. Secondly, for fabrication, we need to split the waveguide into two parts. This should be done along the direction of the current flow to prevent losses in the gap after assembly. If the waveguide is symmetric along the center on the top and bottom walls, we can split the waveguide from the middle to achieve this goal. Longitudinal slots break the symmetry of the waveguide in this direction. Fig. 15 shows one H-shaped slot. We keep the length of the middle line fixed and we change the lengths of the two side arms to achieve the desired radiated power.

The designed antenna is a uniformly excited 36-element linear array. In order to avoid grating lobes, the spacing between the slots is chosen to be 12mm which is smaller than half-wavelength at our operating frequency. In order to have a uniform excitation, the slots that are further from the feed point need to radiate a larger fraction of the incident power. Fig. 16 shows the ratio of the radiated power to the incident power for different arm lengths L for the H-shaped slot. Using this plot, the arm lengths of the slots are given in Table 2 for different slot numbers.

VI. LOSS ANALYSIS

The designed slotted antenna has a series feed network which makes the structure simple. On the other hand, in a series-fed antenna, the loss is accumulated as the wave propagates.

TABLE 2. The arm lengths of the slots for different slot numbers.

Slot number	Arm length L [mm]
1-5	4.4
6-10	4.5
11-15	4.6
16-19	4.7
20-22	4.8
23-25	4.9
26-27	5.0
28-29	5.1
30-31	5.2
32-33	5.3
34	5.4
35	5.5
36	5.6

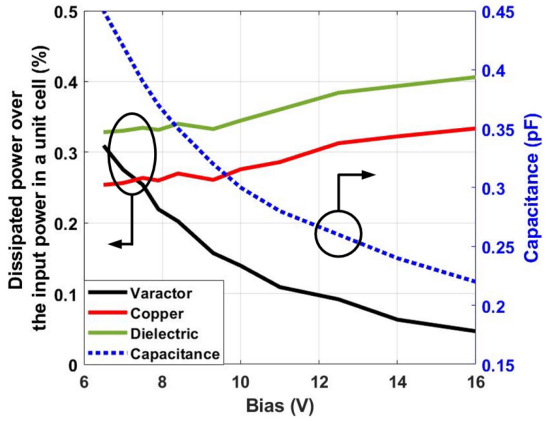

FIGURE 17. Loss analysis in one unit cell.

For this reason, it is necessary to study the different loss mechanisms in the designed waveguide. This can be done by finding the amount of power dissipated in different elements in a unit cell.

Fig. 17 shows the ratio of the dissipated power due to different factors to the input power in a unit cell of the designed waveguide. As shown, dielectric loss is the dominant source of power dissipation throughout the biasing range. This is because the effective traveling length of the wave inside the dielectric is the sum of the lengths of all the dipoles which is much longer than the length of the waveguide. The second dominant source of loss is the ohmic metallic loss. As shown, the dielectric loss and the ohmic metallic loss follow similar trends when the bias voltage is changed. By increasing the bias voltage, β is decreased and so does the wave incident angle on the phase-shifting walls. As a result, the wave bounces more times between the two side walls per unit length which in return, increases the dielectric and ohmic metallic losses. On the other hand, the power dissipated in the varactors has an opposite trend. This is because the quality factor decreases dramatically at lower bias voltages and this makes the varactor loss dominant at voltages below 6 volts.

It is remarkable that contrary to most works on beam-steerable antennas that use varactors as the tunable elements, the varactor loss is not the dominant loss in the designed

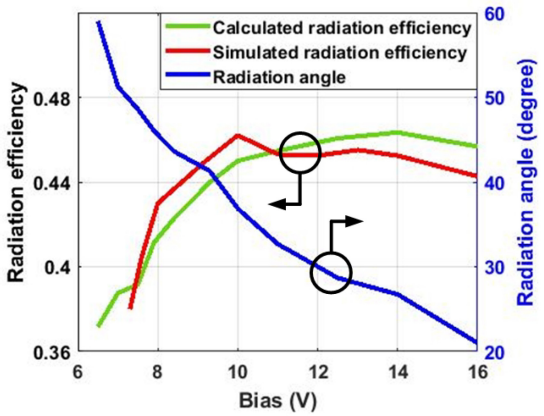

FIGURE 18. Calculated and simulated radiation efficiency vs. the bias voltage and its corresponding radiation angle for the designed waveguide with a length of 13λ at 9.2 GHz.

antenna. This is due to the proposed phase-shifting mechanism in which the phase-shifting walls are placed at the two sides of the rectangular waveguide where the electric field has the least strength. Therefore, this work is advantageous in applications where varactors operate at high frequencies and hence have relatively low quality factors.

Considering all losses in a unit cell and the radiated power from each slot after every 4 unit cells, one can find the radiation efficiency of the designed antenna using equation (21). P_{loss} is the ratio of the dissipated power over the input power in one unit cell as shown in Fig. 17. $P_{r,k}$ is the ratio of the radiated power over the input power for the kth slot as shown in Fig. 16. The number 4 in the power of the first term is due to that fact that the slots are placed after every 4 unit cells.

$$EF = \sum_{k=1}^{N} (1 - P_{loss})^{4k} (1 - P_{r,1}) \cdots (1 - P_{r,k-1}) P_{r,k} \qquad (21)$$

Fig. 18 shows the calculated radiation efficiency using equation (21) as well as the radiation efficiency found by simulating the whole antenna structure. As shown, the radiation efficiency changes from 38% to 46% as we increase the bias voltage from 7 to 16 volts. The quality factor of the varactors drops rapidly as we decrease the voltage which is the reason for lower efficiencies at lower bias voltages. The reason for the slight drop in the radiation efficiency at high bias voltages is that the antenna operates close to the cut-off frequency in this range where the dielectric and ohmic metallic losses increase according to Fig. 17.

In order to study the effect of the distance between the two phase-shifting walls on the loss, one needs to solve equation (13) for different values of the parameter a. Given the operating frequency and the impedance of the phase-shifting walls, the eigenmode solution of (13) for k_x becomes smaller as we increase a. As a result, the longitudinal wave vector is increased and in return, the loss percentage in one unit cell due to different mechanisms decreases. Fig. 19 shows the percentage of different power losses in one unit

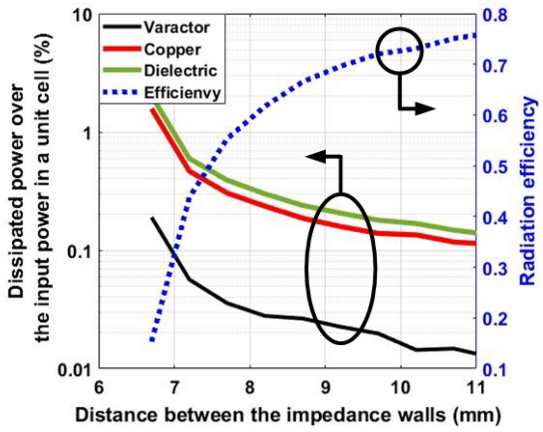

FIGURE 19. Losses and radiation efficiency versus the distance between the two impedance walls.

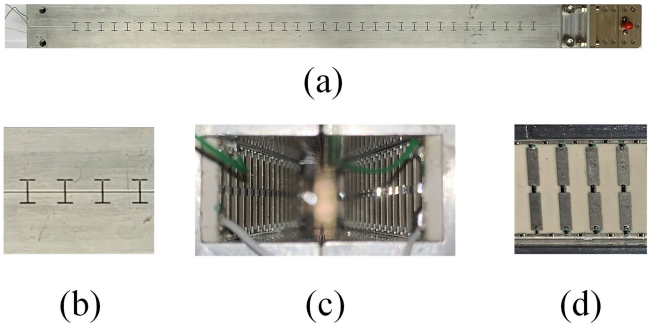

FIGURE 20. a. The fabricated antenna with the WR90-to-coax adapter attached to the right end and the voltage bias wires to the left end. b. A zoomed section showing the H-shaped loaded slots. c. The tapered section at one end of the fabricated antenna. d. A section of the fabricated phase-shifting wall placed inside the antenna.

cell and its resulting radiation efficiency for different values of the distance between the two impedance walls at 9.2 GHz for the bias voltage of 16 Volts. As shown, all losses in a unit cell are decreased as the distance between the two impedance walls is increased.

Comparing Fig. 19 and Fig. 14, one can see the trade-off between the steering range and the radiation efficiency as we change the distance between the two impedance walls. As our goal is to maximize the steering range, we choose 7mm for the distance between the two impedance walls. We could increase the maximum radiation efficiency to 67% if we wanted to limit the steering range to 25° by choosing the distance between the two impedance walls to be 8.7mm.

VII. MEASUREMENT RESULTS

Fig. 20 shows a picture of the fabricated antenna. One end of the antenna is connected to an SMA-to-WR90 adapter for excitation and the other end is used for providing the DC bias voltage to the two tunable impedance walls through two pairs of wires. As the power delivered to the second port is negligible, leaving this end of the antenna open does not introduce considerable reflection to disturb the phase distribution along the waveguide. The length of the fabricated antenna is 509mm, while the effective radiating length is 420mm which is equivalent to 13λ. The difference in the lengths is for the two tapered sections. The width of the structure is 41.4mm while the width of the reconfigurable waveguide is only 10mm. The extra width is for supporting the flanges.

Fig. 21 shows the normalized measured and simulated gain of the antenna for 5 different bias voltages at 9.3 GHz in the E-plane. By changing the bias voltage from 7 to 16 volts, the antenna beam steers from 65° to 22° and its side-lobe level remains less than −9 dB throughout the steering range. The smallest half-power beamwidth (HPBW) of the antenna is 5°. The difference between the measured and simulated gains can be attributed to the ohmic metallic loss due to the gaps between the two parts of the waveguide as well as the flange and the waveguide which cannot be easily included in the simulation. It is worth mentioning that a slight gap between the substrate of the impedance wall and the PEC wall of the waveguide results in a smaller effective distance between the two phase-shifting walls (a). According to Fig. 14, a slight variation in a from the designed value of 7 mm distorts the radiation pattern considerably and results in a decreased gain and the formation of high-level side-lobes. We eliminated this variance by gluing the substrates to the PEC side walls of the waveguide.

As the beam is steered towards larger angles, the pattern changes. The main change is that the half-power beamwidth becomes larger which is consistent with the HPBW approximation (22) where L is the physical length of the antenna, θ is the steering angle, and HPBW is in radians. The term in the denominator of (22) is the effective radiating length of the antenna in terms of the steering angle. The fundamental reason for the increase in the HPBW at larger steering angles, as shown in Fig. 21, is the decrease in the effective radiating length. The drop in the radiation efficiency at lower bias voltages makes the effective radiating length even smaller because of the faster wave attenuation, resulting in a larger HPBW as shown in Fig. 21.d and 21.e.

$$HPBW = \frac{\lambda}{L\,cos(\theta)} \tag{22}$$

The other change in the radiation pattern is the development of a 'shoulder' below −5 dB on the right side of the main beam at larger steering angles as shown in Fig. 21.d and 21.e. This is formed due to the phase variance in the first radiating elements as the shoulder is asymmetric and is only formed to the right side of the main beam. The phase variance can be attributed to the fact that at lower bias voltages, the field configuration is stronger at the impedance surfaces. This makes the dispersion relation and the radiation pattern more prone to any imperfections in the impedance surface including the non-linear behavior of the diodes as well as the finite thickness of the impedance wall. The fact that this is manifested strongly at the first radiating elements giving rise to a shoulder to the right of the main beam is due to the stronger excitation of these radiating elements. This is because the guided wave is attenuated faster at lower

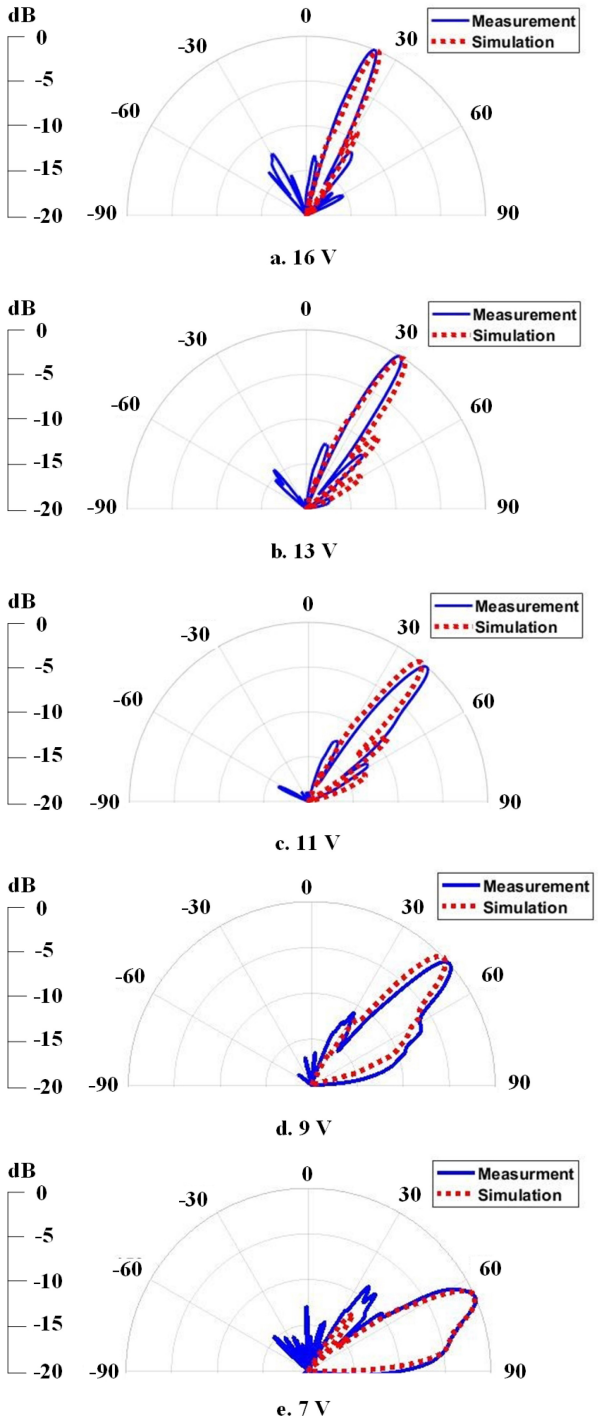

FIGURE 21. Normalized measured and simulated gain of the antenna in the E-plane at 9.3 GHz.

bias voltages, therefore, the first radiating elements have a stronger excitation, hence a stronger effect on the radiation pattern.

In order to compensate for the two mentioned changes in the radiation pattern, one needs to increase the efficiency at lower bias voltages which can be achieved by increasing the distance between the two side impedance walls. However, this will decrease the steering range as discussed before.

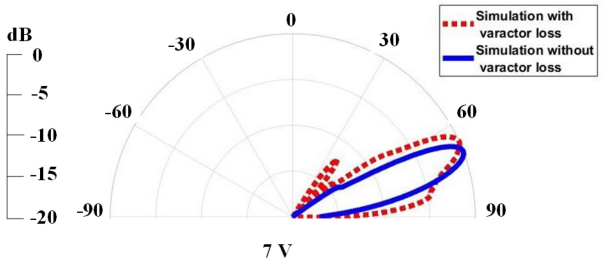

FIGURE 22. Normalized simulated gain of the antenna in the E-plane at 9.3 GHz with and without the varactor loss at 7 Volts.

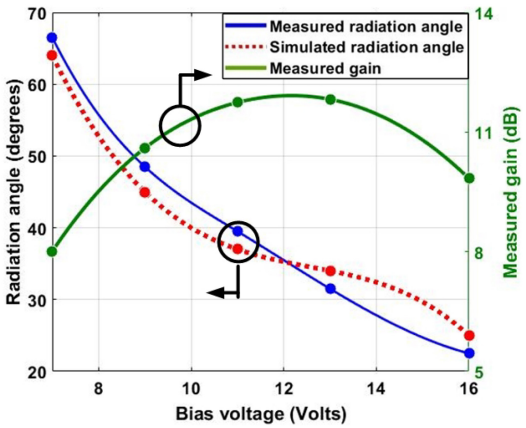

FIGURE 23. Measured and simulated radiation angle versus the bias voltage as well as the corresponding measured gain at 9.3 GHz.

Fig. 22 compares the radiation pattern for the bias voltage of 7 Volts with and without the varactor loss. As shown, eliminating the varactor loss increases the radiation efficiency. As a result, it makes the HPBW smaller and removes the shoulder from the right of the main beam at 7 Volts.

Fig. 23 shows the measured and simulated radiation angle versus the bias voltage as well as the corresponding measured gain. As shown, the gain of the antenna remains within the 3 dB limit of the maximum gain of 11.8 dB at the bias voltage of 13 volts. The drop in the gain at lower bias voltages is due to the decrease in the quality factor of the varactors. On the other hand, at higher bias voltages, the matching is deteriorated as the cut-off frequency of the reconfigurable waveguide is increased and becomes closer to the operating frequency. As shown, the measured and simulated radiation angle versus the bias voltage match well. The slight difference can be attributed to the voltage drop over the DC decoupling resistors. Although the current flow in these resistors is very small, it slightly lowers the effective DC bias voltage of the varactors which in return increases the corresponding radiation angle.

Fig. 24 shows the radiation patterns for different bias voltages at different frequencies. As shown, the antenna steering range varies by changing the frequency of operation which stems from the dispersive nature of the impedance walls. We alleviated the high dynamics of the frequency response of the dipoles by choosing the operating frequency to be away from the resonance frequency of the dipoles. This not only

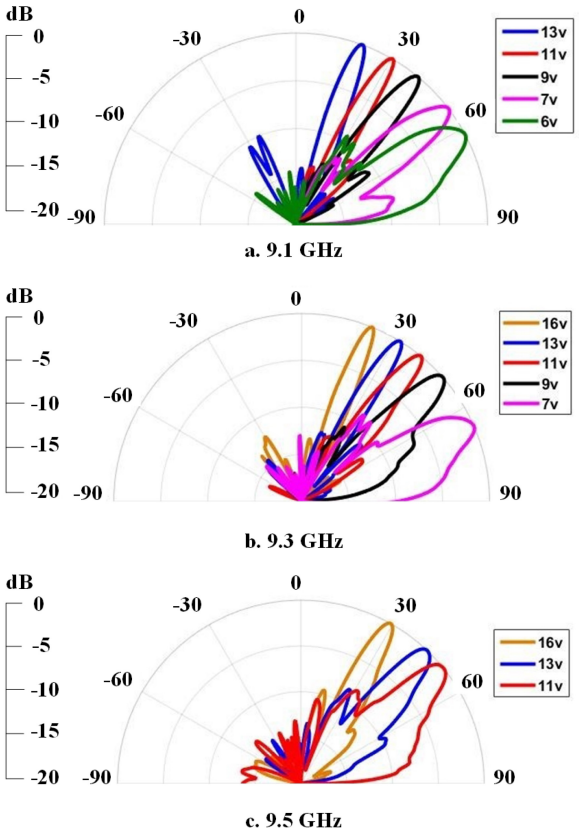

FIGURE 24. Measured normalized radiation patterns at different frequencies.

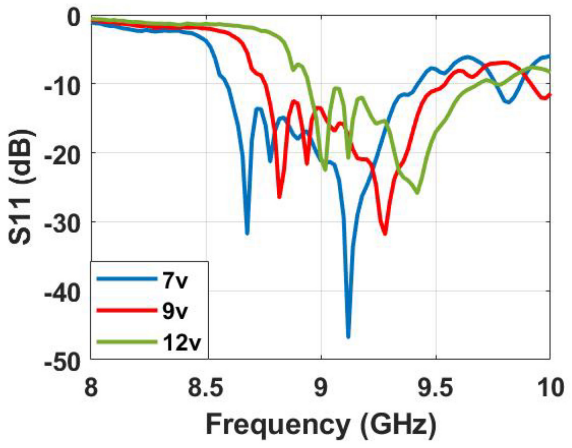

FIGURE 25. Measured S_{11} of the fabricated antenna.

reduces the loss as discussed in the previous section, but also it makes the frequency response more broadband.

The return loss of the fabricated antenna is shown in Fig. 25 for different bias voltages. The measured magnitude of S_{11} for the fabricated antenna is less than -10 dB throughout the steering range and within the operating bandwidth from 9 GHz to 9.5 GHz.

VIII. COMPARISON AND DISCUSSION

The proposed antenna is based on a waveguide fed slot array [21]–[22]. Therefore, the commensurate comparisons should be with scanning waveguide slot arrays and their substrate-integrated waveguide (SIW) counterparts. Nevertheless, we also compare the proposed antenna with some other state-of-the-art fixed-frequency leaky-wave antennas of other kinds (e.g., planar) although such a comparison cannot be exhaustive. However, we exclude discrete beam steering using binary switches as the loss in switches is less than in varactors. Therefore, discrete beam steering can provide higher efficiencies at the cost of discrete scanning instead of continuous scanning as well as a more complex bias circuitry (i.e., each switch needs an individual bias).

Table 3 compares the characteristics of the proposed antenna with those of recent relevant research works. In [27], the lower band operating around 4.25 GHz has a large steering range with a high efficiency. However, both the efficiency and the steering range degrade substantially in the upper band operating around 5.75 GHz. The drop in the efficiency is due to the fact that the quality factor of the varactors decreases at higher frequencies. Nevertheless, the smaller steering range is a result of the smaller capacitance range of the varactors. This is because of the magnified effect of the parasitic inductance on the total impedance of the varactor at higher frequencies. Comparing the performance of this antenna in the second band with that of our proposed antenna shows that the latter can provide twice the steering range and efficiency at a higher frequency using varactors with the same quality factor.

In [28], the antenna radiation efficiency for a wave traveling length of 3.8λ is 60% which would be significantly less if the traveling length was 13λ and the operating frequency was 9.2 GHz as in the case of the proposed antenna.

In [16], a beam-steerable transmitarray with an integrated leaky-wave feed is proposed. The phase-shifting mechanism is localized at each radiating element through two cascaded bridged-T phase-shifters which are biased independently. Therefore, the number of DC bias voltages grows as N^2 where N is the number of radiating elements in each dimension. The varactor loss accounts for 3.2 dB of the total loss which makes it the most significant source of power dissipation in this design. This is contrast to the proposed approach in which the varactor loss is inherently minimized as explained in Section VI. Nevertheless, as the phase-shifting mechanism is localized, the loss does not accumulate by increasing the size of the antenna. However, the complexity of the feed and biasing networks grows rapidly by increasing the size of the antenna. Furthermore, the complexity of the phase-shifters behind each radiating element is considerable.

In [20], a tunable composite right-/left-handed antenna is proposed for beam-steering using GaAs varactors. The antenna has a small electrical length but it can provide a large scanning range through broadside. The antenna has a simple feed and biasing network with two bias voltages. However, due to the relatively low radiation efficiency for even a small electrical length, it is not suitable for applications that require narrow half-power beamwidths and a large electrical length.

TABLE 3. Comparison with other fixed-frequency scanning antenna arrays.

Reference	Freq. [GHz]	Scanning range	Antenna size	Varactor Q factor*	Efficiency	Extrapolated efficiency**	Gain [dB]	Minimum HPBW	Bias voltages
[27] Band 1	4.25	80^o (-34^o – $+46^o$)	4.65λ	3000	80% – 90%	54% – 74%	7 – 12	12^o	1
[27] Band 2	5.75	22^o (-45^o – -23^o)	7.15λ	3000	40% – 50%	19% – 28%	9.5 – 12	8^o	1
[28]	5.5	30^o – 2D (-15^o – $+15^o$)	5.4λ x 5.4λ ***	4000	60%	29%	5 – 16.1	10^o	4
[16]	4.8	90^o – 2D (-45^o – $+45^o$)	3λ x 3λ	4000	25% – 35%	25% – 35%	12.1 – 15.6	19^o	36
[20]	5	69^o (-37^o – $+32^o$)	2.6λ	3000	60%	7.8%	4.4 – 5.7	24^o	2
[19]	5.8	45^o (-16^o – $+29^o$)	6.2λ	500	10% - 20%	0.8% - 3.4%	4 – 8	9^o	1
This Work	9.3	43^o ($+22^o$ – $+65^o$)	13λ	3000	38% – 46%	38% – 46%	8 – 11.8	5^o	1

* Minimum quality factor of the varactor at 1 MHz.

** The efficiency if the antenna length is extended to 13λ (the same length as the proposed antenna) assuming the same attenuation factor.

*** The effective radiating area is less depending on the antenna sectors that are activated.

In [19], a fixed-frequency beam-steerable leaky-wave antenna is proposed using electronically controllable corrugated microstrip line loaded with silicon varactors with relatively lower quality factor compared to other works in Table 3. The proposed antenna operates at 5.8 GHz and its radiation efficiency is between 10% to 20% throughout its operating range. In the paper, it is shown that by including the power dissipation in the varactors, the radiation efficiency drops from 68% to 20% which confirms that the varactor loss is the dominant loss in the designed antenna.

One significant advantage of the proposed antenna is its radiation efficiency. For comparing it in Table 3, we extrapolated the reported radiation efficiency of other works assuming an antenna length of 13λ with the same attenuation factor. As shown in Table 3, the proposed antenna has the highest extrapolated radiation efficiency among the antennas operating higher than 4.5 GHz. This is a significant advantage given the fact that the quality factor of the varactors drops dramatically at higher frequencies according to Fig. 13 which reduces the radiation efficiency. Moreover, contrary to the other research works discussed, the loss in the varactors is the least compared to other loss mechanisms in the designed antenna. Another advantage of the proposed antenna is that the spurious interaction between the electronic control elements and the radiating slots is minimal since the two are physically separated. Moreover, the width of the designed impedance-wall antenna is less than half-wavelength, therefore, they can be arranged side by side to narrow the beam in the H-plane.

IX. CONCLUSION

In this paper we discussed the design and implementation of a new fixed-frequency beam-steerable leaky-wave antenna operating at 9.3 GHz. The phase-shifting mechanism in the designed antenna is through two identical tunable metasurfaces placed on the two sides of the slotted waveguide that provide the desired phase shift to the incident waves. The antenna can steer its beam from 65° to 22° when the bias voltage is changed from 7 to 16 volts. The designed antenna has a radiating length of 13λ leading to a 5° HPBW. The antenna simulated radiation efficiency changes from 46% to 38% throughout the steering range. One important characteristic of the designed antenna is the fact that the power dissipated in the varactors is less than the dielectric and ohmic metallic loss thanks to the proposed phase-shifting mechanism through the two impedance walls on the two sides of the waveguide where the strength of the electric field is low. This enables using the varactors at higher frequencies where their quality factor drops considerably compared to lower frequencies. This makes the proposed antenna an advantageous alternative in applications where the operating frequency is relatively close to the self-resonance frequency of the varactor. As the antenna has a simple feed network and bias circuitry with a relatively high efficiency, it can be used where simple antenna length extension is needed to achieve a larger gain and a narrower beamwidth. In addition, the width of the designed antenna is smaller than half-wavelength which makes it possible to place the same antennas side-by-side to narrow the beam in the non-scanning plane.

REFERENCES

[1] K.-C. Huang and Z. Wang, "Millimeter-wave circular polarized beam-steering antenna array for gigabit wireless communications," *IEEE Trans. Antennas Propag.*, vol. 54, no. 2, pp. 743–746, Feb. 2006.

[2] C. Huang, W. Pan, X. Ma, B. Zhao, J. Cui, and X. Luo, "Using reconfigurable transmitarray to achieve beam-steering and polarization manipulation applications," *IEEE Trans. Antennas Propag.*, vol. 63, no. 11, pp. 4801–4810, Nov. 2015.

[3] J. Schoebel *et al.*, "Design considerations and technology assessment of phased-array antenna systems with RF MEMS for automotive radar applications," *IEEE Trans. Antennas Propag.*, vol. 53, no. 6, pp. 1968–1975, Jun. 2005.

[4] M. Sazegar *et al.*, "Beam steering transmitarray using tunable frequency selective surface with integrated ferroelectric varactors," *IEEE Trans. Antennas Propag.*, vol. 60, no. 12, pp. 5690–5699, Dec. 2012.

[5] D. Sievenpiper *et al.*, "Electronic beam steering using a varactor-tuned impedance surface," in *Proc. IEEE AP-S Symp. Antennas Propag.*, Boston, MA, USA, Jul. 2001, pp. 174–177.

[6] H. Moghadas, M. Daneshmand, and P. Mousavi, "MEMS-tunable half phase gradient partially reflective surface for beam-shaping," *IEEE Trans. Antennas Propag.*, vol. 63, no. 1, pp. 369–373, Jan. 2015.

[7] C. W. Jung, M.-J. Lee, G. P. Li, and F. D. Flaviis, "Reconfigurable scan-beam single-arm spiral antenna integrated with RF-MEMS switches," *IEEE Trans. Antennas Propag.*, vol. 54, no. 2, pp. 455–463, Feb. 2006.

[8] S. Xiao, C. Zheng, M. Li, J. Xiong, and B.-Z. Wang, "Varactor-loaded pattern reconfigurable array for wide-angle scanning with low gain fluctuation," *IEEE Trans. Antennas Propag.*, vol. 63, no. 5, pp. 2364–2369, May 2015.

[9] C.-M. Liu, S.-Q. Xiao, H.-L. Tu, and Z. Ding, "Wide-angle scanning low profile phased array antenna based on a novel magnetic dipole," *IEEE Trans. Antennas Propag.*, vol. 65, no. 3, pp. 1151–1162, Mar. 2017.

[10] Y. Ji, L. Ge, J. Wang, Q. Chen, W. Wu, and Y. Li, "Reconfigurable phased-array antenna using continuously tunable substrate integrated waveguide phase shifter," *IEEE Trans. Antennas Propag.*, vol. 67, no. 11, pp. 6894–6908, Nov. 2019.

[11] C. L. Holloway, E. F. Kuester, J. A. Gordon, J. O'Hara, J. Booth, and D. R. Smith, "An overview of the theory and applications of metasurfaces: The two-dimensional equivalents of metamaterials," *IEEE Antennas Propag. Mag.*, vol. 54, no. 2, pp. 10–35, Apr. 2012.

[12] A. Epstein and G. V. Eleftheriades, "Passive lossless huygens metasurfaces for conversion of arbitrary source field to directive radiation," *IEEE Trans. Antennas Propag.*, vol. 62, no. 11, pp. 5680–5695, Nov. 2014.

[13] K. Chen *et al.*, "A reconfigurable active Huygens' metalens," *Adv. Mater.*, vol. 29, May 2017, Art. no. 1606422.

[14] J. Y. Lau and S. V. Hum, "Reconfigurable transmitarray design approaches for beamforming applications," *IEEE Trans. Antennas Propag.*, vol. 60, no. 12, pp. 5679–5689, Dec. 2012.

[15] J. Y. Lau and S. V. Hum, "A wideband reconfigurable transmitarray element," *IEEE Trans. Antennas Propag.*, vol. 60, no. 3, pp. 1303–1311, Mar. 2012.

[16] J. G. Nicholls and S. V. Hum, "Full-space electronic beam-steering transmitarray with integrated leaky-wave feed," *IEEE Trans. Antennas Propag.*, vol. 64, no. 8, pp. 3410–3422, Aug. 2016.

[17] D. K. Karmokar, Y. J. Guo, P.-Y. Qin, S.-L. Chen, and T. S. Bird, "Substrate integrated waveguide-based periodic backward-to-forward scanning leaky-wave antenna with low cross-polarization," *IEEE Trans. Antennas Propag.*, vol. 66, no. 8, pp. 3846–3856, Aug. 2018.

[18] A. Ohadi and G. V. Eleftheriades, "A frequency-scanned slow-wave waveguide antenna at millimeter-wave frequencies," *IEEE Access*, vol. 8, pp. 174910–174921, 2020.

[19] M. Wang, H. F. Ma, H. C. Zhang, W. X. Tang, X. R. Zhang, and T. J. Cui, "Frequency-fixed beam-scanning leaky-wave antenna using electronically controllable corrugated microstrip line," *IEEE Trans. Antennas Propag.*, vol. 66, no. 9, pp. 4449–4457, Sep. 2018.

[20] S.-L. Chen, D. K. Karmokar, Z. Li, P.-Y. Qin, R. W. Ziolkowski, and Y. J. Guo, "Continuous beam scanning at a fixed frequency with a composite right-/left-handed leaky-wave antenna operating over a wide frequency band," *IEEE Trans. Antennas Propag.*, vol. 67, no. 12, pp. 7272–7284, Dec. 2019.

[21] R. A. Gilbert, "Waveguide slot antenna arrays," in *Antenna Engineering Handbook*. New York, NY, USA: McGraw-Hill, Apr. 2007, ch. 9.

[22] A. Ohadi and G. V. Eleftheriades, "A beam-steerable slotted waveguide antenna with tunable impedance walls," in *Proc. IEEE AP-S Symp. Antennas Propag.*, Montreal, QC, Canada, Jul. 2020, pp. 489–490.

[23] A. Epstein and G. V. Eleftheriades, "Huygens' metasurfaces via the equivalence principle: Design and applications," *J. Opt. Soc. Amer. B*, vol. 33, no. 2, pp. A31–A50, Feb. 2016.

[24] R. B. Dybdal, L. Peters, and W. H. Peake, "Rectangular waveguides with impedance walls," *IEEE Trans. Microw. Theory Techn.*, vol. MTT-19, no. 1, pp. 2–8, Jan. 1971.

[25] K. Kurokawa, "Electromagnetic waves in waveguides with wall impedance," *IRE Trans. Microw. Theory Techn.*, vol. 10, no. 5, pp. 314–320, Sep. 1962.

[26] C. Balanis, *Antenna Theory: Analysis and Design*. Hoboken, NJ, USA: Wiley, Apr. 2015.

[27] M. Wang, H. F. Ma, H. C. Zhang, W. X. Jiang, and T. J. Cui, "A dual-band electronic-scanning leaky-wave antenna based on a corrugated microstrip line," *IEEE Trans. Antennas Propag.*, vol. 67, no. 5, pp. 3433–3448, May 2019.

[28] R. Guzmán-Quirós, A. R. Weily, J. L. Gómez-Tornero, and Y. J. Guo, "A Fabry–Pérot antenna with two-dimensional electronic beam scanning," *IEEE Trans. Antennas Propag.*, vol. 64, no. 4, pp. 3433–3448, Apr. 2016.

AMIRMASOUD OHADI (Student Member, IEEE) received the B.A.Sc. degree in electrical engineering from the University of Tehran and the M.A.Sc. degree in electrical engineering from Cornell University. He is currently pursuing the Ph.D. degree in electrical engineering with the University of Toronto.

He was selected as an ECE Fellow at Cornell University from 2014 to 2015, academic year and he received the Spork Analog Design Fellowship from Cornell University in spring 2016. His current research interests include antenna design, microwave and RF systems, and periodic structures.

GEORGE V. ELEFTHERIADES (Fellow, IEEE) received the M.S.E.E. and Ph.D. degrees in electrical engineering from the University of Michigan at Ann Arbor, Ann Arbor, MI, USA, in 1989 and 1993, respectively.

From 1994 to 1997, he was with the Swiss Federal Institute of Technology, Lausanne, Switzerland. He is currently a Professor with the Department of Electrical and Computer Engineering, University of Toronto, Toronto, ON, Canada, where he holds the Canada Research/Velma M. Rogers Graham Chair of Nano- and Micro-Structured Electromagnetic Materials. He is currently leading a group of graduate students and researchers in the areas of electromagnetic and optical metamaterials, and metasurfaces, antennas and components for broadband wireless communications, novel antenna beam-steering techniques, far-field superresolution imaging, radars, plasmonic and nanoscale optical components, and fundamental electromagnetic theory. He is a recognized international authority and pioneer in the area of metamaterials. These are man-made materials which have electromagnetic properties not found in nature. He introduced a method for synthesizing metamaterials using loaded transmission lines. Together with his graduate students, he provided the first experimental evidence of imaging beyond the diffraction limit and pioneered several novel antennas and microwave components using these transmission-line based metamaterials. His research has impacted the field by demonstrating the unique electromagnetic properties of metamaterials; used in lenses, antennas, and other microwave and optical components to drive innovation in fields, such as wireless and satellite communications, defence, medical imaging, microscopy, and automotive radar.

Prof. Eleftheriades received the Ontario Premier's Research Excellence Award and the University of Toronto's Gordon Slemon Award in 2001, and the 2018 Research Leadership Award from the University of Toronto. He received an E. W. R. Steacie Fellowship from the Natural Sciences and Engineering Research Council of Canada in 2004. Paper that he coauthored have received numerous awards, such as the 2009 Best Paper Award from the IEEE MICROWAVE AND WIRELESS PROPAGATION LETTERS, twice the R. W. P. King Best Paper Award from the IEEE Transactions on Antennas and Propagation in 2008 and 2012, and the 2014 Piergiorgio Uslenghi Best Paper Award from the IEEE ANTENNAS AND WIRELESS PROPAGATION LETTERS. He is the recipient of the 2008 IEEE Kiyo Tomiyasu Technical Field Award, the 2015 IEEE John Kraus Antenna Award, and the 2019 IEEE AP-S Distinguished Achievement Award. He served as the General Chair of the 2010 IEEE International Symposium on Antennas and Propagation held in Toronto, ON, Canada. He served as an Associate Editor for the IEEE TRANSACTIONS ON ANTENNAS AND PROPAGATION (AP). He also served as a member of the IEEE AP-Society Administrative Committee from 2007 to 2012, and was an IEEE AP-S Distinguished Lecturer from 2004 to 2009. In 2009, he was elected a Fellow of the Royal Society of Canada.